Auroral heating of plasma patches due to high-latitude reconnection

Joaquin Diaz Pena[1], Joshua L. Semeter[1], Yukitoshi (Toshi) Nishimura[1], Roger Varney[2], Ashton S Reimer[2], Marc R. Hairston[3], Matthew David Zettergren[4], Michael Hirsch[1], Olga P. Verkhoglyadova[5], Keisuke Hosokawa[6], and Kazuo Shiokawa[7]

[1]Boston University
[2]SRI International
[3]University of Texas at Dallas
[4]Embry-Riddle Aeronautical University
[5]Jet Propulsion Laboratory, California Institute of Technology
[6]University of Electro-Communications
[7]Institute for Space-Earth Environmental Research, Nagoya University

November 24, 2022

Abstract

This study exploits the volumetric sampling capabilities of the Resolute Bay Incoherent Scatter Radar (RISR-N) in collaboration with all-sky imagery and in-situ measurements (DMSP) to examine the interplay between cold plasma transport and auroral precipitation during a high-latitude lobe reconnection event on the dawn side. The IMF had an impulsive negative excursion in B_z embedded within a prolonged period of $B_z>0$ and $B_y<0$. The combined effects of transport and magnetic stress release associated with a reconnection pulse resulted in a co-mingling of plasma patches and soft electron precipitation, creating regions of elevated electron density and temperature. Altitude profiles of ionospheric parameters extracted in the rest frame of the drifting patch showed an increase in T_e above 200 km and N_e below 250 km (both hallmarks of soft precipitation), while also showing small and predictable changes in N_e near the F-region peak over the 34-minute duration of the event. For the first time, we identified that the simultaneous appearance of elevated T_e and elevated F-region N_e (i.e., a 'hot patch'), thus providing a new formation process for hot patches. The physics-based GEMINI model was used to explore the response to the observed precipitation as a function of altitude and time. Enhancements in N_e in the topside ionosphere (e.g., DMSP altitudes) are caused by upward ambipolar diffusion induced by ionospheric heating and not impact ionization. The study highlights the importance of densely distributed measurements in space and time for understanding both mesoscale and small-scale ionospheric dynamics in regions subject to complex forcing.

Auroral heating of plasma patches due to high-latitude reconnection

Joaquín Díaz Peña[1], Joshua Semeter[1], Yukitoshi Nishimura[1], Roger Varney[2],

Ashton Reimer[2], Marc Hairston[3], Matthew Zettergren[4], Michael Hirsch[1],

Olga Verkhoglyadova[5], Keisuke Hosokawa[6], Kazuo Shiokawa[7]

[1]Department of Electrical Engineering and Center for Space Physics, Boston University, Boston MA

[2]SRI International, Menlo Park CA

[3]William B. Hanson Center for Space Sciences, The University of Texas at Dallas, Dallas TX

[4]Embry-Riddle Aeronautical University, Daytona Beach FL

[5]Jet Propulsion Laboratory, California Institute of Technology, Pasadena, CA

[6]Department of Communication Engineering and Informatics, The University of Electro-Communications,

Tokyo Japan

[7]Institute for Space-Earth Environmental Research, Nagoya University, Nagoya Japan

Key Points:

- The 4-D ionospheric response to high-latitude reconnection is studied using the RISR facility, OMTI all-sky imager, and DMSP spacecraft.
- A reconnection pulse forced the co-mingling of an F-region patch and a polar cap arc, creating a common region of elevated Ne and Te.
- Numerical modeling predicted enhanced Ne at DMSP (800 km) due to upward diffusion.
- The observed reconnection-induced heating of a cold patch is a new mechanism for hot patch generation.

Abstract

This study exploits the volumetric sampling capabilities of the Resolute Bay In-coherent Scatter Radar (RISR-N) in collaboration with all-sky imagery and in-situ mea-surements (DMSP) to examine the interplay between cold plasma transport and auro-ral precipitation during a high-latitude lobe reconnection event on the dawn side. The IMF was characterized by an impulsive negative excursion in B_z embedded within a pro-longed period of $B_z > 0$ and $B_y < 0$. The combined effects of transport and magnetic stress release associated with a reconnection pulse resulted in a co-mingling of plasma patches and soft electron precipitation, creating regions of elevated electron density and temperature. Altitude profiles of ionospheric parameters extracted in the rest frame of the drifting patch showed a contemporaneous increase in T_e above 200 km and N_e be-low 250 km (both hallmarks of soft precipitation), while at the same time showing small and predictable changes in N_e near the F-region peak over the 34-minute duration of the event. For the first time we identified that the simultaneous appearance of elevated T_e and elevated F-region N_e (i.e., a 'hot patch'), thus providing a new formation process for hot patches. The physics-based GEMINI model was used to explore the response to the observed precipitation as a function of altitude and time. Enhancements in N_e in the topside ionosphere (e.g., DMSP altitudes) are caused by upward ambipolar diffusion induced by ionospheric heating and not impact ionization. The study highlights the im-portance of densely distributed measurements in space and time for understanding both mesoscale and small-scale ionospheric dynamics in regions subject to complex forcing.

1 Introduction

Magnetic reconnection represents a fundamental mode of energy transfer into and out of the geospace system. Many phenomena of the polar ionosphere may be directly traced to reconnection, including the formation of fast flow channels (Zou et al., 2015), poleward moving auroral forms (Oksavik, Moen, & Carlson, 2004), poleward boundary intensifications (PBI's) along the nightside separatrix (De la Beaujardiere et al., 1994)(Zou et al., 2016), and ionospheric upflow in the cusp (Strangeway et al., 2000) and nightside auroral regions (Semeter, Heinselman, Thayer, Doe, & Frey, 2003). From an energy per-spective, the merging of the solar wind and magnetosphere constitutes a magnetospheric generator, establishing the electric fields that drives often complex convection patterns in the ionosphere. For periods of southward interplanetary magnetic field (IMF), obser-

vational evidence suggests that, on average, there is a balance between magnetopause reconnection on the dayside and magnetotail reconnection on the nightside (Dungey, 1961). When the IMF is northward directed, reconnection occurs differently from the southward IMF. Regions that are favorable to reconnection shift from the dayside magnetopause to the lobe magnetic field lines poleward of the cusps (Gosling, Thomsen, Bame, Elphic, & Russell, 1991). The formation of reverse convection cells, multi-cell convection patterns, and soft discrete arcs in the polar cap are some of the consequences that arise due to the reversal in orientation of the IMF B_z component from negative (southward) to positive (northward) (Fuselier, Petrinec, & Trattner, 2000; Lockwood & Moen, 1999; Øieroset, Sandholt, Denig, & Cowley, 1997; Onsager, Scudder, Lockwood, & Russell, 2001).

Ground-based observations have shown that reconnection is not a continuous smooth process, and the existence of reconnection pulses is expected regardless of the IMF orientation (Fear, Trenchi, Coxon, & Milan, 2017). For southward IMF conditions, pulsed reconnection on the dayside is one of the major agents for the creation of F-region plasma patches (or polar cap patches)(Crowley, 1996; Tsunoda, 1988). Patches are enhanced density regions that are generated in the dayside and convected across the polar cap towards the night side, with reconnection serving as the trigger for patch generation and segmentation (Basu & Valladares, 1999; Carlson, 1994, 2007, 2012; Lockwood & Carlson, 1992). These areas of higher plasma density then drift and deform in a manner consistent with general convection streamlines established by electrostatic potential contours. For northward IMF, polar cap patches are still expected (Coley & Heelis, 1998; McEwen & Harris, 1996; Zhang et al., 2016), particularly if there are sudden changes of B_z (Valladares et al., 1998) and in the presence of precipitation Oksavik et al. (2006). In general, the solar wind does not smoothly vary, and rapid transients in IMF can impart rapid reconfigurations of convection patterns in the ionosphere (Lu et al., 2002; Ruohoniemi & Greenwald, 1998)

Despite the fact that many studies on the mechanisms of polar ionospheric structure, the relative importance of transport, chemistry, diffusion, current systems, and their relation to magnetospheric drivers remain a subject of debate (Moen et al., 2013). From the perspective of magnetospheric drivers, the major challenge lies in reconstructing a four-dimensional space-time dynamic from measurements that are sparse and/or limited in coverage. Progress has been made in recent years by combining coordinated measures from LEO satellites, ground-based cameras, the SuperDARN HF radar network, and the

Advanced Modular Incoherent Scatter (AMISR) installation at Resolute Bay, Canada (referred to as RISR-N) (Dahlgren et al., 2012; Gillies et al., 2018; Koustov et al., 2020; Lyons et al., 2011; Perry et al., 2015). The electronic scanning capability of the two co-located RISR systems (RISR-N and RISR-C) is particularly important for remote sensing of the highly dynamic ionospheric conditions occurring at the footprint of reconnection events.

This paper exploits the volumetric sampling capabilities of RISR-N to observe the evolution of plasma density structures, auroral ionization, and auroral heating during a series of pulsed reconnection events along the dawnside separatrix. In conjunction with optical measurements and satellite data, we can analyze the existence of reconnection by looking at the interplay between auroral forms, particle precipitation, and plasma transport. Of particular interest is the ability to reconstruct ionospheric parameters in the convecting (Lagrangian) reference frame to trace the dynamic evolution of patches. We show that the formation of soft and structured precipitation and the $B_\perp$ acceleration of plasma patches are two consequences of the same magnetospheric process – namely, the release of magnetic stress resulting from reconnection. The effect of the IMF orientation is also essential because reconnection is happening primarily at dawn rather than midnight. For the event presented in this study, the interplay of these responses dictates the density and thermal structure of the ionosphere in these regions. The co-existence of high F-region density and elevated electron temperature in these regions (i.e., "hot patches") are a natural and expected consequence of this interplay. First-principles modeling is used to elucidate the relationship between F-region plasma observed by RISR-N and the topside (800 km) plasma measured by DMSP.

2 Instruments and setting

The case study examined in this work occurred on 24 January 2012. This period was selected based on the fortuitous availability of concurrent measurements by DMSP, the OMTI auroral imager, and the electronically scannable RISR-N facility during an extended interval where the open-closed field-line boundary was observed by all diagnostics. For context, Figure 1 summarizes the solar wind magnetic field measured at L1. The solar wind data was obtained from the NASA/GSFC's OMNI data set through OMNIWeb and have been time-shifted to the Earth's bow shock 1. The transfer of solar wind transients to the ionosphere from this point depends on factors such as the IMF orien-

¹²⁰ tation and the mode of magnetosphere-ionosphere coupling (Ruohoniemi & Greenwald,

¹²¹ 1998; Watanabe et al., 2005), but is expected to be of order a few minutes. The period

¹²² beginning at ∼9:45 UT was characterized by a steady IMF B_z positive and B_y negative

¹²³ – conditions favorable for a contracted auroral oval and high-latitude reconnection (Mi-

¹²⁴ lan, Hubert, & Grocott, 2005). An exception was a sharp dip and sign reversal in B_z at

¹²⁵ ∼11:15 UT. This dynamic change is considered significant in understanding the nature

¹²⁶ of the observed ionospheric response, as discussed later.
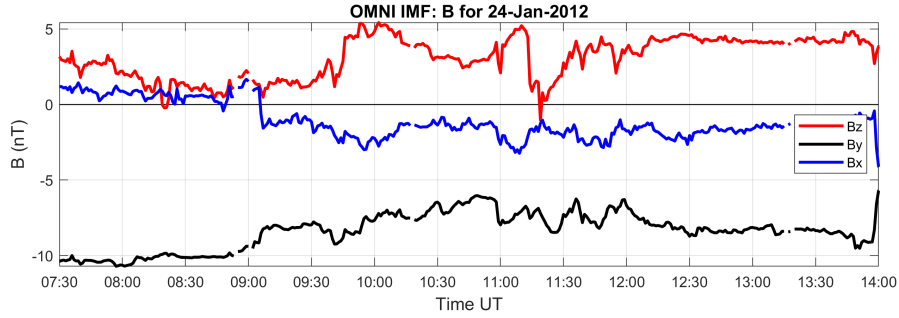

Figure 1: OMNI solar wind measurements for 24 January 2012

¹²⁷ **RISR-N**. The RISR-N facility (74.73N, 94.91W) provided the crucial spatially and

¹²⁸ temporally resolved data for this study. During the period of interest, RISR-N operated

¹²⁹ with 42 beams in a spatial pattern depicted in the horizontal coordinate system in Fig-

¹³⁰ ure 2a. Beam-patterns such as this enable construction of time-dependent three-dimensional

¹³¹ volumetric images of ionospheric several ionospheric state parameters that are observed

¹³² by RISR-N: N_e, T_e, T_i, and V_{LOS}. Note that spacing between spatial samples and hor-

¹³³ izontal coverage both increase with increasing altitude with sample spacing and horizon-

¹³⁴ tal coverage that increase with increasing altitude (c.f. Figure 2b). The uncertainties in

¹³⁵ observed state parameters depend on the number of samples integrated per position and

¹³⁶ the backscattered power, which decreases with ionospheric density and range (c.f Fig-

¹³⁷ ure 1 in Davis and McCrea (2004))(Farley, 1969). For this experiment, we used a 2-minute

¹³⁸ integration period which provides 171 pulses per beam position.

¹³⁹ Figure 2b shows an example of the sampled density field with each sample displayed

¹⁴⁰ as a color-coded dots. The samples are then used in a 3D nearest-neighbor interpolation

¹⁴¹ in Figure 2c (see, e.g., Dahlgren et al., 2012; Semeter et al., 2009) The interpolated data

¹⁴² product allows flexibility in visualizing the evolution of plasma. E.g., plasma motion may

be estimated from sequential images as well as from bulk Doppler shift in the backscatter spectrum. Also, it is now possible to cut through the data in any direction, particularly in the direction of the magnetic field, which is nearly 90° in elevation at the RISR-N location. This enables us to study plasma dynamics in the convecting frame of reference. These capabilities will be discussed further in Section 3.1.

(a)   (b)   (c)
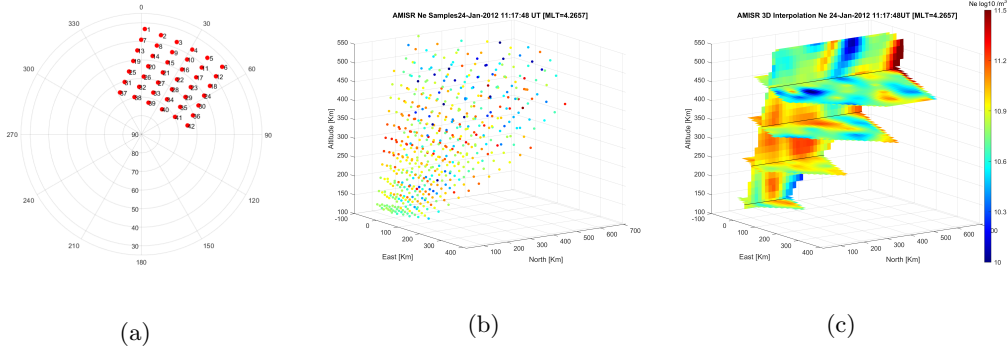
Figure 2: a) RISR-N beam pattern in horizon coordinates for 24 January 2012, b) Example of three-dimensional sampling acquired from this mode, c) Example of three-dimensional interpolation product

DMSP. The Defense Meteorological Satellite Program (DMSP) is a constellation of LEO sun-synchronous satellites in a dusk-dawn polar orbit at a nominal altitude of ∼833 km. Originally developed primarily for weather monitoring, the DMSP spacecraft include a variety of plasma instruments as well. This work made use of the thermal plasma monitor (SSIES) and the precipitation particle spectrometer (SSJ/5)..

The DMSP satellites orbit with a velocity of ∼7.4 km/s, which means that they cross the polar cap on a timescale similar to the timescales associated with changes in the convection pattern. Thus the spacecraft measurements contain an ambiguous mixture of spatial and temporal effect, which must be partitioned using additional diagnostics.

For this study, we used the thermal plasma monitor and the precipitation particle spectrometer instruments, commonly known as the SSIES and SSJ/5 instruments respectively. DMSP satellites F15 through F18 were available during the interval under

161 study, with the F16 satellite passing closes to RISR-N, however, we ignored F15 data since

162 it does not provide SSJ/5 data

163 We mostly use SSIES instrument suite (Rich & Hairston, 1994), which is composed

164 of several elements, such as the ion drift meter (IDM) and the retarding potential an-

165 alyzer (RPA). Both of these sensors were built to work on plasma with predominantly

166 O^+ ions. IDM measures the ion drift velocity perpendicular to the track and in the hor-

167 izontal (Vy) and vertical (Vz) directions. On the other hand, the RPA is responsible for

168 measuring ion temperature (T_i), ratio of $O+$ to $H+$ or $He+$, and the ion drift velocity

169 along the satellite track (V_x).

170 The precipitation boundary identification strategy developed by Newell, Feldstein,

171 Galperin, and Meng (1996) made it possible to find the approximate location of the po-

172 lar cap boundary, or open-closed boundary (OCB), as well as the auroral zone among

173 several others, by using the SSJ5 sensor and particle precipitation spectrum. Kilcom-

174 mons, Redmon, and Knipp (2017) also presented a method for using both particle pre-

175 cipitation and magnetometer data to identify the auroral zone. Both techniques helped

176 define a more precise general location of the OCB for this study, which allowed us to de-

177 termine what type of aurora was present at higher latitudes. This helped identify the

178 existence of discrete arcs either inside or outside the polar cap and their relation to the

179 drift velocities measured during the satellite's orbit.

180 **OMTI.** Co-located with the RISR facility is an all-sky imager for studying aurora

181 and airglow. The imager is part of the Optical Mesosphere Thermosphere Imagers (OMTI)

182 managed by the Nagoya University (Shiokawa et al., 1999; Shiokawa, Otsuka, & Ogawa,

183 2009), and has been operational since 2005. The filters in place are for the green line (557.7nm),

184 red line (630nm), thermospheric oxygen (777.4 nm), sodium line, and hydrxyl line. OMTI

185 registers red line images every 2 minutes with 30 seconds of exposure each (Hosokawa

186 et al., 2009, 2006). In this work, the OMTI 630 nm images are used to provide space-

187 time context to assist in the interpretation of direct plasma measurements by RISR, and

188 orbital measurements of particles and drifts by DMSP.

3 Observations

3.1 RISR-N and OMTI

Figure 3 shows two different representations of ionospheric variation extracted from the four-dimensional RISR-N data, as discussed in Section 2, for the period 11-14 UT on 24 January 2012. Figure 3(a–c) plots vertical cuts of N_e, T_e, and T_i, which is a good approximation of the field aligned direction due to the $\sim90°$ magnetic field dip angle. Several patches can be seen passing through the zenith of RISR-N, with an F region peak density approximately at 300 km for each one. This range-time summary of the data is used to emphasize the unique capabilities of the AMISR radar later on. Note that the patches between 11:20 UT and 11:58 UT are accompanied by high electron temperature within the patches. This phenomenon has been named 'hot patch' in Zhang et al. (2017), which attributed the elevated T_e as evidence of soft auroral precipitation, and hence conjectured that patch generation by means other than dayside plasma transport may be at play. This notion was later updated by Ma et al. (2018), where the relation between T_e and T_i became the key to differentiate between a hot patch and a classical patch, by stating that if inside a patch the ratio $T_i/T_e < 0.8$ applies, we are in the presence of a hot patch. Ma et al. (2018) also implies that hot patches are related to precipitation and bursty plasma flow and represent the initial creation phase of patches, becoming classical patches as they decrease their temperature. The incoherent scatter radar observations provided by RISR-N are the only measurements that enable the detailed examination of these dynamics that we now present.

Using Figure 3(a–i) together emphasizes the unique capabilities of and fundamental contribution of RISR-N to this study. The 4-D imaging (3D space + time) allows us to develop an empirical understanding of the differences between these classes of patches. The low-temperature patch occurring near 12:00UT is theorized to not be large but moving slowly and occupying the whole field of view of RISR-N, and due to its time, it could have been caused by the sudden change in polarity of B_z (Valladares et al., 1998) and a reconfiguration of the convection in the polar cap. Both before and after 12:00UT patches show ionization below 200 km, signaling the existence of precipitation. This also highlights the importance of a full 3D space + time analysis of the event. The full analysis makes it clear that due to the location of the vertical profiles (100km east and 150km north of RISR-N), several patches look like hot patches, which could mean they are in
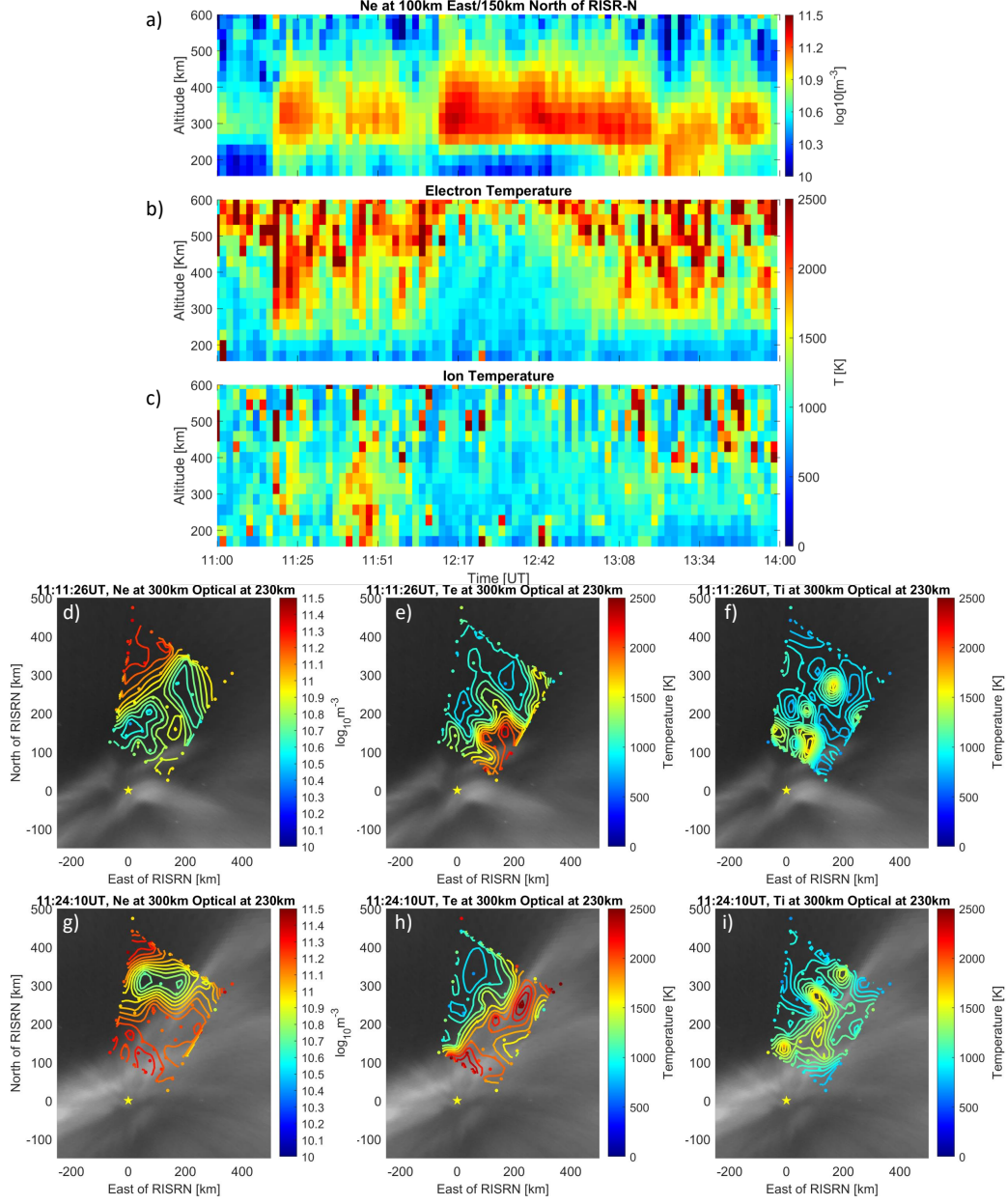
Figure 3: (a–c) Interpolated plasma parameters from RISR-N. These are displayed as a purely vertical profile 100km east and 150km North of RISR-N (d-i) Horizontal cuts of plasma parameters at 300km altitude with OMTI red line filter included. (d–f) Shows patch entering the field of view of RISR-N as a cold patch. (g–i) Shows patch become a hot patch with high T_e and low T_i. This behavior repeats for all patches that have low altitude density at around 200km

the initial creation stage of a patch. Horizontal cuts of the 3D interpolated data reveal this is an incorrect conclusion in this case. Figure 3(d–f) shows horizontal cuts of N_e, T_e, and T_i at 300 km extracted from interpolated RISR-N data. The contours are spatially registered with oxygen 630-nm (redline) images from OMTI (shown in gray scale), assuming an emission altitude of 230 km. The spatial coordinates in the figure indicate distance east and north of RISR-N, with the location of RISR-N highlighted by a yellow star at the origin.

In Figure 3(d–e) it is possible to see how one of these patches comes into the field of view with cold plasma temperatures. This would make that patch a fully formed cold patch. Complementing these RISR-N observations with additional instrumentation, we can unambiguously classify the type of patch and its possible origin.

It is worth repeating that an analysis of this event that only uses single altitude profiles can incorrectly conclude that there are several hot patches in their initial state as defined by Ma et al. (2018). Therefore it is important to note that an analysis that considers the the time evolution of the patches as they move through the d spatial field of view of RISR-N iis required to correctly conclude that all patches enter the field of view as mature cold patches and become heated via interaction with the local precipitation environment (supported by movie MS1). Figure 3(g–i) then shows the same patch minutes later as it interacts with the aurora and becomes a hot patch through the interaction with the aurora since its electron temperature is much higher than its ion temperature. This analysis also reveals that there are likely several different mechanisms for producing hot patches, which is something future studies should attempt to identify using the same 4D analysis performed in this study.

For a better understanding of how the patches move with respect to the auroral forms during the event, we analyze both RISR-N and OMTI observations together. Figure 4 follows the patch shown at 11:20UT in Figure 3a during twelve contiguous 2-minute intervals during the period 11:11 to 11:30 UT. Figures 4a–4j follow the same characteristics as Figure 3(d–i).

The white arrows are scaled line-of-sight velocity vectors extracted from the bulk Doppler shift of the ISR spectrum. The velocity vectors shown have been scaled by dividing by the cosine of its elevation angle, such that the length represents the horizontal component of the velocity towards or away from the origin of a plane at 300-km al-

253   titude (assuming velocites are primarily horizontal – a reasonable assumption at 300 km

254   altitude near the geomagnetic pole). Only velocity vectors with relative error <40% are

255   included in the figure.

256   Note that the measurements with errors below this threshold are co-incident with

257   regions of high plasma density, which corresponds to large radar SNR, as expected.

258   Figures 4k–4t show vertical cuts of N_e through the same interpolated volume. This

259   view reveals the north-south motions of plasma structures at different altitudes. Of par-

260   ticular interest is the plasma patch centered at ∼300-km (solid ovals), and the ioniza-

261   tion from soft precipitation extending down to ∼140-km (dashed ovals).

262   The motions of the patch are revealed in two ways in Figure 4: through the den-

263   sity structures (color contours), and through the bulk plasma Doppler shift (white ar-

264   rows). The time-sequential visualizations in Figure 4 show that the patch had an almost

265   purely southward trajectory during this interval. As such it will cross the auroral pole-

266   ward boundary if it keeps that trajectory. The radar is approximately at 4.5 MLT, which

267   means that the patches are moving towards dawn. There is a visible acceleration in the

268   patch velocity between 11:17UT and 11:19UT (4d to 4e) where the center of the patch

269   moves almost 100 km in a span of 2 minutes, which corresponds to almost 830 m/s. This

270   velocity compares well with the scaled LOS velocities observed by RISR-N that show the

271   increase size at 11:17UT.

272   Starting in panel 4n until panel 4t the appearance of low altitude high-density plasma

273   is visible, which coincides with the expansion of the auroral arc poleward as seen in the

274   OMTI data, and thus its origin can be attributed to precipitation. The dynamic struc-

275   ture of the 630-nm auroral forms in this region are suggestive of electron acceleration

276   by inertial Alfvénic waves. Such waves would be expected for an impulsive release of mag-

277   netic tension associated with a reconnection pulse (e.g., Keiling, 2009).

278   The fast movement eastward correlates with the high velocity inside the arc, as mea-

279   sured by the RISR-N LOS velocity vectors. This could mean smaller convection cells nested

280   within the larger one. There is perfect coincidence between the aurora moving poleward,

281   the patch accelerating southward, and the generation of low altitude density. The patch

282   then carries this low altitude density out of the field of view as the aurora moves equa-

283   torward. After the patch and aurora are aligned (panel 4g onward), it is impossible to
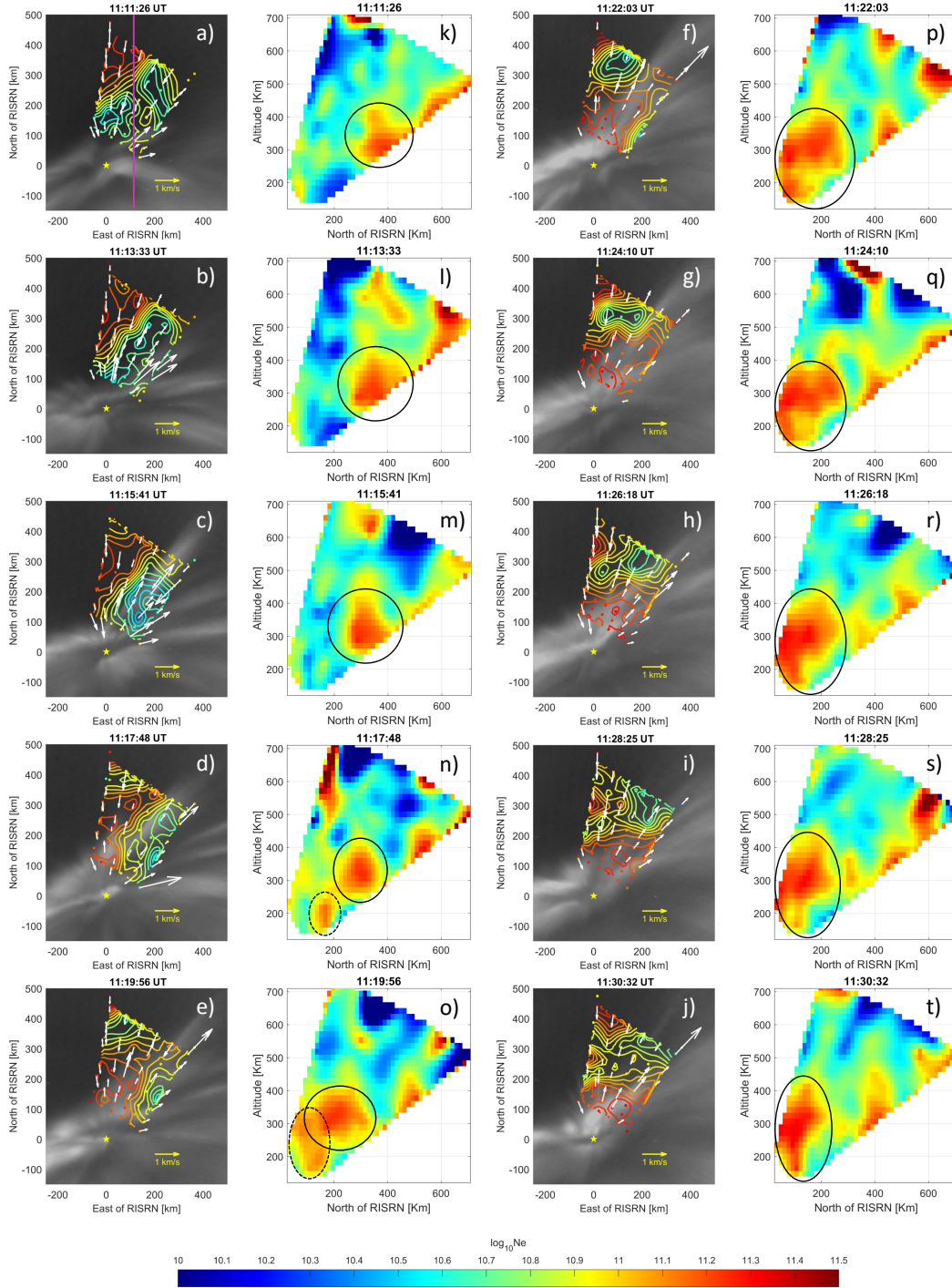
Figure 4: a–j) horizontal cuts of ionospheric density (N_e) at 300 km altitude (color contours) overlain on 630-nm redline images (grayscale) mapped at 230km. White arrows represent line-of-sight velocities measured projected to a plane at 300-km altitude, as described in the text. k–t) North-south vertical density cuts 100km east of RISR-N represented by the pink line in a), showing the relative motion of a plasma patch (solid ovals) and a region of plasma production by precipitation (dashed ovals). Purple line on a) represents the location of vertical cuts

differentiate precipitation-generated plasma and pre-exisiting patch plasma in RISR-N observations. By plotting horizontal cuts of the RISR-N data at lower altitudes, it is only possible to observe how the low altitude electron density enhances when the aurora expands and brightens. This perspective shows once again why this 4D approach is vital to differentiate between a hot patch as the initial stage of patch creation or an interaction between a mature cold patch and soft precipitation.

Further insight can be obtained by following the evolution of ionospheric parameters in the frame of reference of the advecting patch, i.e., the Lagrangian reference frame. Figure 5 shows a time-sequence of vertical profiles of N_e and T_e over the interval 11:00 to 11:34 UT (darker to lighter color). The profiles were extracted by performing a spacial average of the parameters over the area of enhanced density. As such, the profiles illustrate how the plasma properties are evolving within the patch on average. Each profile represents a 2-min integration, and the each profile is color-coded to indicate the progression of time using dark red to light yellow. The black profiles show the quiescent background state prior to the patch event, chosen at the time with lowest background density.

Figure 5 shows that N_e and T_e were relatively constant within the patch prior to encountering the region of auroral precipitation, indicated where profiles are red, with the decrease in electron density in time associated with recombination of the background ionosphere. At 11:24UT the patch accelerated into the region of soft precipitation, indicated where the profiles are yellow, where we see elevated F-region T_e, and a build-up of new plasma density below 250 km. These changes are consistent with the presence of an incident electron precipitation energy spectrum with broad energy distribution below $\sim$300 eV.

The observations provide strong evidence for a dynamic interplay between patch transport and soft auroral precipitation initiated by reconnection, which results in a region of prior elevated upper F-region N_e and elevated F-region T_e that are not causally related. Thus, in this case the presence of a 'hot patch' does not indicate the initial creation of a mature patch, but is rather the result of a mature cold patch that has been subjected to auroral heating. The field-of-view of RISR-N is insufficient to track these dynamics further. Future studies using combined observations from RISR-N and the southward pointed RISR-C facility will certainly contribute to enhanced understanding.
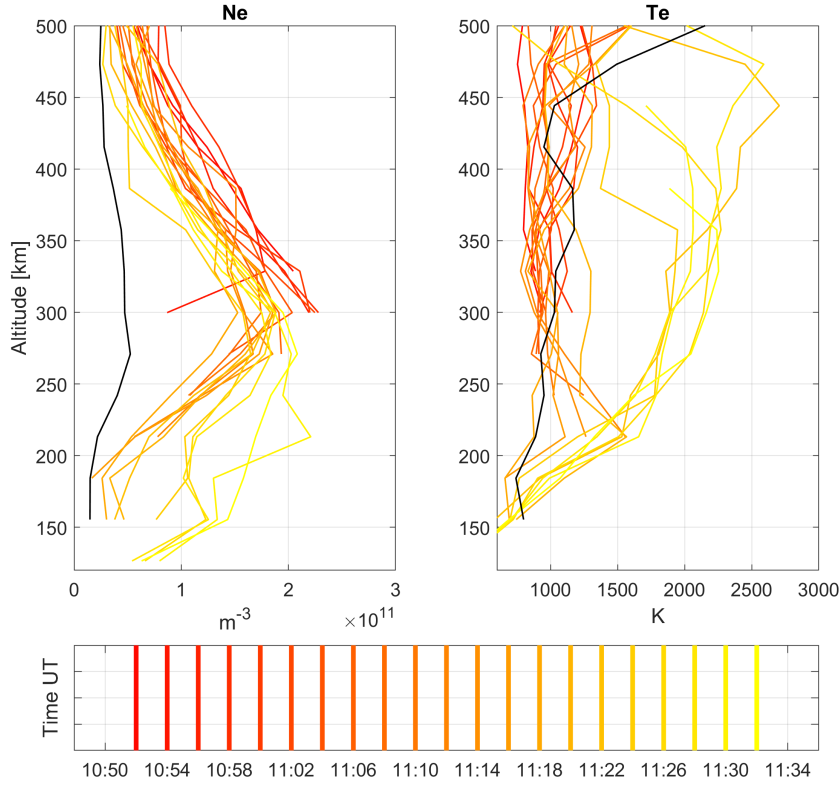
Figure 5: Altitude profiles taken from RISR-N interpolated data that follow the center of the polar cap patch as it moves across the field of view of RISR-N. Times goes as the color goes from darker to lighter, with black lines representing the no-patch background. The increasing ionization in the 150-to-250-km altitude range and the elevated T_e throughout the ionosphere are consequences of the sudden appearance of soft precipitation in the patch frame of reference. The magnetic field line is assumed vertical. Incomplete profiles are due to variations in altitude coverage within the probed volume as the structures drift through (see Fig. 2).

3.2 Global context from DMSP and Weimer

Figure 6 shows the DMSP F16 satellite pass over the polar cap in magnetic coordinates. Overlaid with the SSIES sunward velocity data is an OMTI 630-nm image with the RISR-N field-of-view at 230 km (nominal 630-nm emission altitude) indicated by the yellow trapezoid. The integration interval for the OMTI image corresponds to the 30 seconds highlighted in red in the SSIES data, supporting the RISR-N observations of large

sunward velocities within the arc region. This auroral arc appears to be inside the polar cap and the polar cap looks highly reduced in size, which can be explained by the fact that we have a $B_z > 0$ event (Carlson, 1994; Ismail & Meng, 1982; Valladares, Carlson Jr, & Fukui, 1994). The shape of the optical signature seen in the middle of the FOV of OMTI looks like a polar cap arc seen during the northward IMF conditions as discuss by Hosokawa et al. (2020). In particular, we often see this kind of Sun-aligned structure elongating toward the cusp during periods of horse-collar aurora (Hones Jr, Craven, Frank, Evans, & Newell, 1989).

Figure 6: DMSP F16 orbit over the polar cap for 24 January 2012. Perpendicular lines to the orbit represent horizontal velocity in the sunward direction, with the red lines representing the integration time of the red line filter in OMTI. RISR-N is represented by a star and yellow lines form its field of view at a nominal red-line altitude of 230km

Time series data are shown in Figure 7, with SSIES and SSJ5, plotted. SSJ/5 is capable of measuring both ion and electron precipitation in the 30 eV to 30 keV range

(Redmon, Denig, Kilcommons, & Knipp, 2017). Using the electron energy flux and the empirical boundary model of Newell et al. (1996) , it is possible to roughly approximate the location of the OCB at roughly 11:57:35UT. The auroral zone is also identified by the > 10 keV precipitating electrons between 11:57UT and 12:01UT. There are several regions of soft precipitation inside the polar cap, which explains the existence of the auroral arc over RISR-N field of view measured by the red line filter (100 to 300eV approximately). DMSP F16 observes a polar cap patch after the observation of density at 11:49UT of $10^{9.5}$m^{-3}, with a maximum density of $10^{10.5}$m^{-3} at 11:53UT. This is almost one order of magnitude higher than the low density region surroundings. This patch also coincides with the reversal in velocity, now pointing strongly anti-sunwards and thus moving the patch through the polar cap. Currently, it is not possible to link this particular patch at high altitude with any of the patches observed by RISR-N.
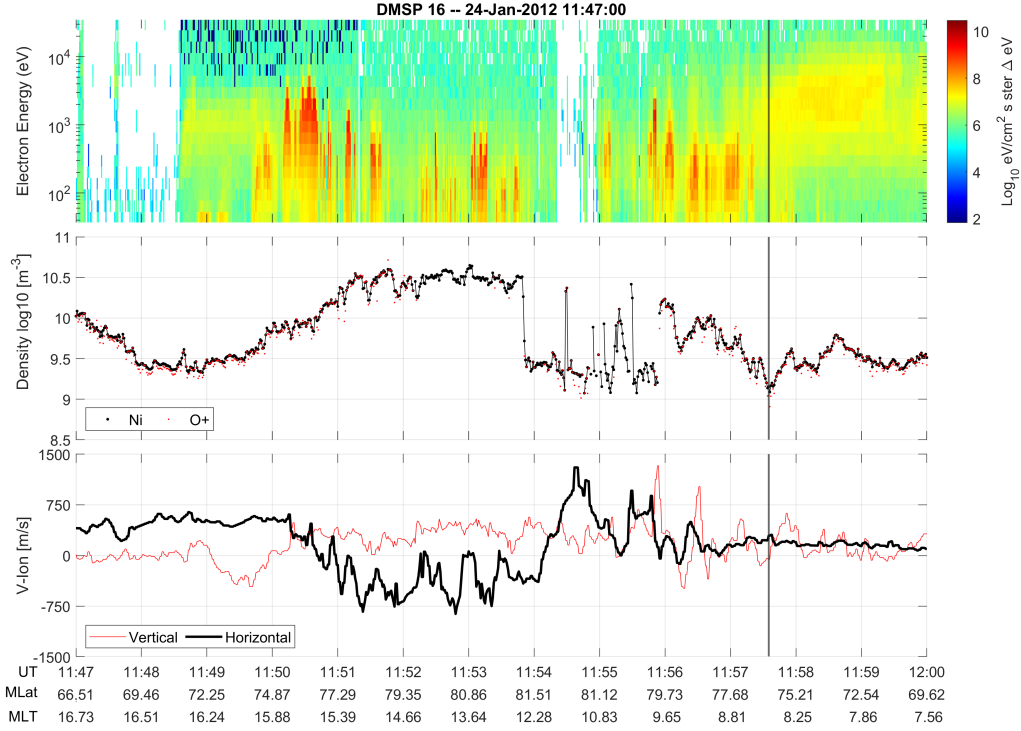

Figure 7: DMSP F16 measurements of precipitating electrons, oxygen ratio and ion velocities over the polar cap

For this particular day, the IMF B_z was slightly northward and B_y was strongly negative as obtained from OMNI (WIND level 3 high resolution data). By following the

results of Heppner and Maynard (1987) and Potemra, Zanetti, Bythrow, Lui, and Iijima (1984), we expect that the global convection pattern was most likely a distorted two-cell pattern. This pattern also allows for the existence of polar cap arcs as discussed by So- jka, Zhu, Crain, and Schunk (1994). We ran the Weimer model for several times for this date utilizing the online CCMC tool and OMNI inputs. These Weimer models runs are empirically-derived statistical electric potential maps for the high-latitude ionosphere de- veloped by Weimer (1995) and can help us approximate the overall large scale convec- tion pattern. Figure 8 shows plots of the Weimer potential result for the current day at different times during the RISR-N experiment:

a) 10:11UT Pre event image, no visible aurora, dawn side is trying to split into to sep- arate convection cells as one would expect in a constant positive B_z scenario.

b) 10:48UT Initial brightening of the aurora and contraction of the polar cap.

c) 11:11UT First appearance of the polar cap arc forming on the night/predawn side of the polar cap.

d) 11:34UT Fully form polar cap arc extending from the night side to the field of view of RISR-N. What was previously an anti sun-ward convection has now turned dawn- ward.

4 Discussion

The observations presented herein reveal how the combined effects of plasma trans- port and particle precipitation, initiated by high-latitude reconnection, can create regions of elevated ionospheric density and temperature consistent with the notion of a 'hot patch' (Ma et al., 2018; Zhang et al., 2017). This is consistent with our observations. The find- ings are enabled by the volumetric sampling capability of RISR-N. In particular, Ma et al. (2018) study shows that hot patches are more frequently observed near the polar cap boundary, whereas cold patches are more frequently observed in the central polar cap. Furthermore, it shows most hot patches are observed on the dusk side, but some hot patches are observed on the dawn side like our case. Vertical parameter profiles extracted from interpolated data (Figure 3) showed multiple small-scale patches co-located with elevated electron temperature in the in the 11:15–12:00 UT interval and again in the13:10–14:00 interval, with a continuous cold plasma enhancement in between. Three-dimensional time- dependent analysis showed that the F-region features were transported into the RISR-

Weimer 24-Jan-2012 10:11:00UT, Radar 3.1452MLT   Weimer 24-Jan-2012 10:48:00UT, Radar 3.7468MLT

Weimer 24-Jan-2012 11:11:00UT, Radar 4.1361MLT   Weimer 24-Jan-2012 11:34:00UT, Radar 4.5253MLT
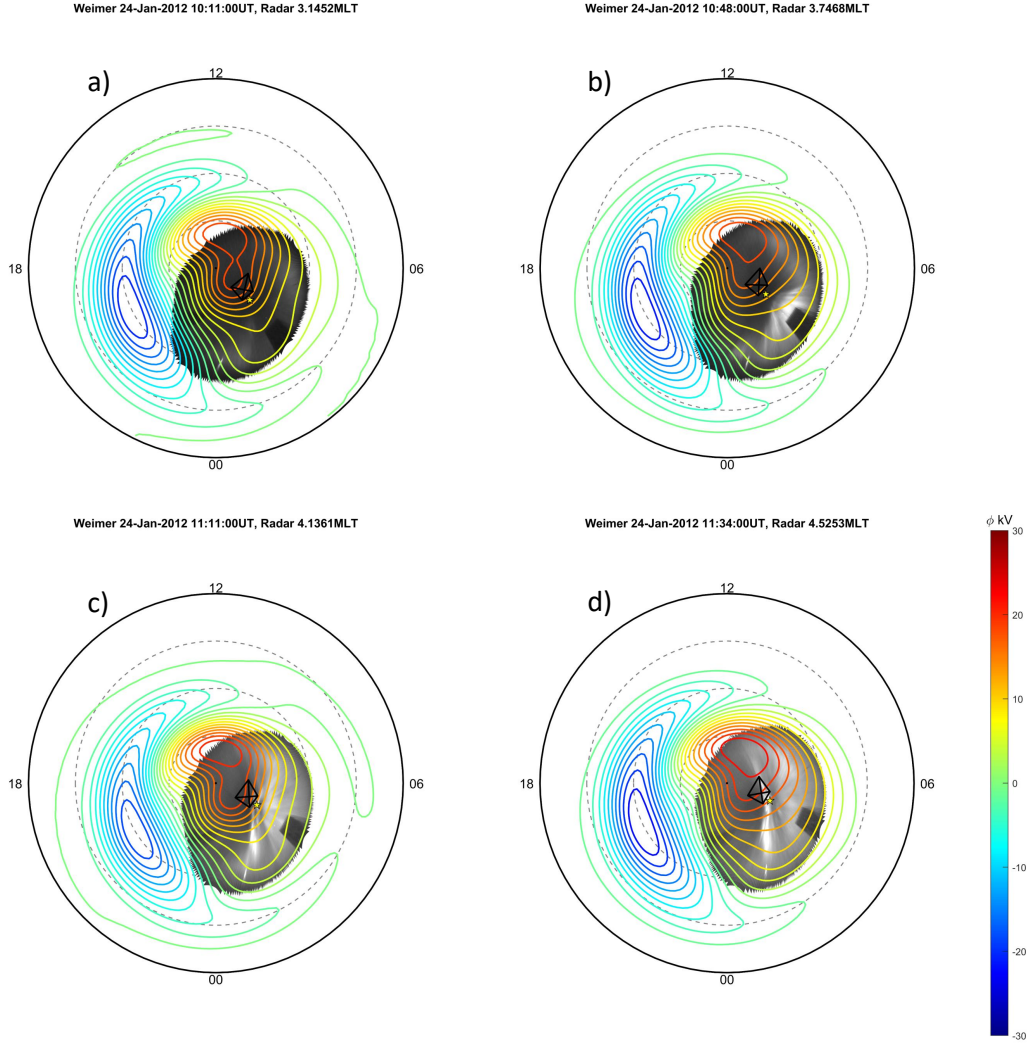
Figure 8: (a–d) Electric potential over the polar cap from the Weimer Models run over-lapped with closest OMTI red line image. It clearly shows a two-cell convection pattern with a central anti-sunward channel. There is no symmetry from dawn to dusk. The yellow star represents the location of AMISR at the moment of measurement. Dark black lines represent the field of view of RISR-N at 300km

377   N fov and into the regions of soft precipitation, rather than produced locally. The ev-
378   idence is well summarized in movie MS1 included as supporting information, which shows
379   the combined OMNI (solar wind), RISR-N (ionosphere), OMTI (aurora), and Weimer
380   (convection) perspectives. In what follows we provide some context for the evidence, and

381 use physics-based modeling to help understand the time scales and expected signatures

382 at low-Earth orbit (e.g., DMSP).

4.1 Relation to solar wind drivers

384 Figure 1 showed that during the hours preceding 11:15UT on 24 January 2012, the

385 IMF B_z was positive, varying between 1 and 5 nT, while B_y was negative increasing steadily

386 (to first order) from -10 to -6 nT (Figure 1). The Weimer modeled convection pattern

387 (Figure 8 and supporting movie MS1) exhibited expected behaviors for these conditions,

388 with a contracting dawnside convection cell and indications of bifurcation of the dawn-

389 side into smaller cells. Line-of-sight ion velocities imaged by RISR-N (Figure 4) were con-

390 sistent with Weimer predictions – i.e., velocities have a persistent equatorward compo-

391 nent poleward of the auroral boundary, but a persistent sunward component equator-

392 ward of the auroral boundary. On the other hand, these velocities were not consistent

393 with observed movements of density features in the same regions, as they move south-

394 ward. This can be explained by two possible factors: reconnection is pushing plasma across

395 field lines through a tangential electric field thus creating the southward movement in-

396 side a convection pattern that is exactly as Weimer presents, or since Weimer is a large

397 scale model small scale variations are not accounted for, which is what RISRN could be

398 measuring in this instance.

399 The aurora that formed within the RISR-N fov at ∼11:07 UT in Figure 4 was char-

400 acterized by dynamic rayed structures dominated by 630-nm redline emission. Mapped

401 projections of the full all-sky field-of-view, shown in Figure 6 and supporting movie MS1,

402 revealed these features to comprise a sun-aligned arc. The IMF conditions for this event

403 – $B_z > 0$, $B_y < 0$, $B_x > 0$ – were favorable for the formation of small-scale sun-aligned

404 arcs (Crooker, 1986; Kullen, Brittnacher, Cumnock, & Blomberg, 2002). At ∼11:15 UT,

405 B_z transitioned rapidly from 5 to -1 nT. This was followed ∼2 min later by a simulta-

406 neous brightening of the arc and equatorward acceleration of the patch across the pre-

407 cipitation boundary, as revealed by Figure 4. These two responses occurred in perfect

408 synchrony. The rapid response of the magnetosphere-ionosphere system to such solar wind

409 transients is well known, and has been investigated in observational (Ruohoniemi & Green-

410 wald, 1998) and modeling (Lu et al., 2002) studies.

4.2 Role of High-latitude Lobe Reconnection

The role of high-latitude reconnection in the formation of sun-aligned arcs has been investigated in some detail (see, Hosokawa et al., 2020, and references therein). This event meets the criteria for the tail reconnection during IMF northward non-substorm intervals (TRINNI) model proposed by Milan et al. (2005). In this model, the polar cap becomes bifurcated into two compartments, and lobe reconnection results in a transfer of open flux from one polar cap compartment to another. The lifetime and migration of the resulting sun-aligned arc depends on continued lobe reconnection and B_y variations. For the present case the negative transient in B_z at 11:15 UT is conjectured to have produced an impulsive increase in reconnection rate, which resulted in acceleration of the plasma patch into the reconnection footprint.

The creation of soft but structured precipitation from reconnection is also expected. A lobe reconnection pulse introduces free energy in the Lagrangian (plasma rest) frame in the form of magnetic tension. This free energy is dissipated through the excitation of small-scale inertial Alfvén waves which accelerate electrons (e.g., Keiling, 2009, and references therein). The rayed morphology of the aurora, often observed in active polar cap arcs, is qualitatively similar to poleward boundary intensifications (PBIs) (Semeter, Heinselman, Sivjee, Frey, & Bonnell, 2005) and auroras associated with substorm expansion (Dahlgren, Semeter, Marshall, & Zettergren, 2013), both of which are associated with Aflvénic electron acceleration. The correlation of flow bursts and particle precipitation in polar cap auroras has also been investigated directly using measurements from the FAST satellite (Bonnell et al., 1999). Figure 7 shows a similar correlation between flow enhancements and soft precipitation throughout the polar cap. The four-dimensional view of the evolving ionospheric state by RISR-N provides critical evidence needed to disentangle the various processes at play.

The effects of lobe reconnection on a drifting plasma patch are best understood by tracking properties in the patch reference frame. Figure 5 shows the the ability to extract this perspective over a substantial regional volume is one advantage of an electronically scannable ISR. Figure 5 showed that the precipitation increased plasma production below 300 km, while simultaneously elevating T_e throughout the ionosphere. These effects are the expected responses to an intense flux of soft electrons ($\lesssim$200 eV) associated with Alfvénic particle acceleration (Semeter & Zettergren, 2014). An important ob-

servation is that the introduction of soft precipitation did not increase the peak patch density at ∼300 km. In fact, the density above 300 km can be seen to decrease slowly over time. This response is expected due to continued recombination and upward diffusion due to the plasma heating.

4.3 GEMINI Modeling

In order to better understand the time and altitude dependencies of the response, we have employed physics-based modeling. The numerical model used is the "Geospace Environment Model for Ion-Neutral Interactions" (GEMINI) based on the model described by Zettergren and Semeter (2012) and expanded by (Zettergren et al., 2014; Zettergren, Semeter, & Dahlgren, 2015; Zettergren & Snively, 2013, 2015). The model encompasses a system of fluid equations (Blelly & Schunk, 1993; Schunk, 1977) describing the ionospheric plasma utilizing the first three moments of the Boltzmann equation (mass, momentum, and energy) for each relevant species, and it is self-consistently coupled to an electrostatic treatment of auroral and neutral dynamo currents. The release of GEMINI used for this work uses the suprathermal electron transport code GLOW (Solomon, 2017)[and references therein] to specify auroral ionization and heating rates. This is a newly developed capability as prior version of GEMINI used semi-empirical models of ionization.

Oksavik et al. (2006) shows how soft electron fluxes found in the cusp or the polar ionosphere can produce islands of enhanced density consistent with our accepted definition of a plasma patch. It is also important to fully understand how dynamic processes in the lower ionosphere (observed by RISR-N) affect the ambient plasma observed in low Earth orbit (e.g., by DMSP at 800 km). To address these issues, the following strategy was employed. We set the initial background N_E profile to the pre-event background (no patch) in Figure 5 (black curve). We then applied an incident Maxwellian electron flux to the GEMINI upper boundary. The average energy and differential number flux were initially set based on DMSP particle measurements near the auroral arc at 11:56–11:57 UT (Figure 7) and adjusted in order to match the observed time-dependent T_e and N_e profiles observed by RISR-N (Figure 5).

We conducted several model runs with varying constraints utilizing Version v0.14.2. Figure 9 summarizes the results that best matched observations (incident Maxwellian

474   spectrum with average energy 330 eV and energy flux $0.4 mW/m^2$). More results are dis-

475   played in the supporting information Figure S1 to S8 for several energy averages. The

476   source was turned on at 11:10 UT and turned off again at 11:20 UT. This duration is

477   somewhat arbitrary for the present purposes, but consistent with expected exposure time

478   of an ionospheric parcel to the precipitation. Several points are made from this run. First,

479   the time to reach steady-state density is about 2 min at 250 km, and decreases with de-

480   creasing altitude as expected. This is consistent with observations in Figure 4 and 5, pro-

481   viding some confidence that we are driving the model with a plausible parameter set.

482   Second, note that the T_e rises almost immediately at ∼200 km, with higher altitudes re-

483   sponding somewhat more slowly. This is also consistent with observed profiles in Fig-

484   ure 5. This effect occurs as the result of the interplay between conduction, convection,

485   and collisional heating by secondaries at the stopping altitude. Second, note that the plasma

486   production for this flux is below the F-region peak at 300 km, while the T_e enhancement

487   extends throughout the ionosphere. Thus this flux has only a minor effect on N_e at patch

488   altitudes. These responses are expected for soft electron fluxes in the <1 keV range (Seme-

489   ter & Zettergren, 2014), and are both consistent with observed behaviors (Figure 5). Thirdly,

490   after the source is removed, F-region densities return to their initial state in ∼15 min.

491   And lastly, note that the ion temperature is affected very little by the precipitation. This

492   is also expected as there is no applied electric field applied and, hence, no frictional heat-

493   ing.

494   In summary, a 330-eV Mawellian with 0.4-mW/m² average flux produces the key

495   behaviors observed in Figures 4 and 5. Turning to the topside, at 800 km we see that

496   electron heating results in an increase in T_e of ∼1000 K during the application of the source.

497   There is also an increase in N_e at this altitude that is lagged by ∼4-min from the time

498   of application of the source at 11:10 UT. There is no collisional production at these al-

499   titudes, the enhanced N_e is due to the upward ambipolar diffusion produced by the elec-

500   tron partial pressure gradient. Also note that the N_e returns to its initial quiescent state

501   ∼7 min after the source is removed. Thus there is no long-term transportable effect pro-

502   duced in the topside ionosphere.

503   Figure 9 supports the conclusion that precipitation can produce ∼1000-K enhance-

504   ments in T_e (factor 2 above background) and order-$10^{10} m^{-3}$ enhancements in N_e (fac-

505   tor ∼10 above background) at 800-km DMSP altitudes, irrespective of the presence of

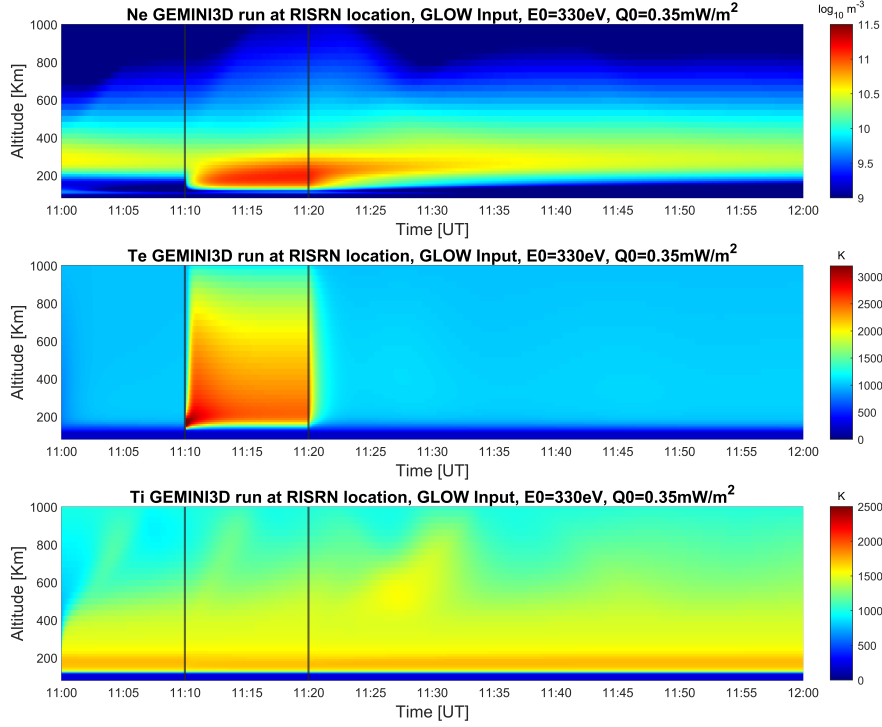506   a plasma patch in the conjugate F-region. The topside signatures observed in this event

Figure 9: GEMINI3D run utilizing a Maxwellian spectrum for the precipitating electrons. E0 of 330eV and energy flux of $4mW/m^2$ were used as taken from DMSP measurements closest to the arc. The time selected corresponds with the UT from the event at 11UT. The range time plot was build by taking the central bin of each time step to simulate what happens right below a stream of precipitating electrons. Precipitation is turned on at exactly 11:10UT and turned off at 11:20UT as marked by black lines

are consistent with parameters identified as a hot patch by Zhang et al. (2017) and Ma et al. (2018). Thus care must taken when inferring lower ionospheric dynamics based on observations at DMSP altitudes. Furthermore, the presence of an F-region patch within a region of soft precipitation and enhanced T_e does not necessarily indicates patch production via precipitation. Transport of a cold plasma patch into a region of intensifying soft precipitation is an expected consequence of lobe reconnection. This presents a way in which a fully mature cold patch can then become a hot patch due to auroral precipitation.

5 Conclusions

We have exploited the four-dimensional (space+time) imaging capabilities of the RISR-N facility to observe ionospheric dynamics in the vicinity of a high-latitude reconnection event. An isolated region of elevated electron temperature and elevated electron density can appear through a co-mingling of transport and precipitation effects, both natural consequence of lobe reconnection. This shows how a fully matured patch can become a cold patch through this method. First-principles modeling was carried out using constraints extracted from RISR-N observations in the lower ionosphere and precipitating electron spectra provided by DMSP SSJ across the polar cap during this period. The results show that the application of a 330-eV Maxwellian incident flux with 0.4 mW/m^2 net energy flux for a few minutes will produce signatures at 800 km that are consistent with reports of a 'hot patch' (e.g., increase in T_e by 1000 K, increase in N_e by factor $\sim$10). This response is not due to impact ionization and occurs irrespective of the presence or not of a plasma patch in the conjugate F-region. The response is due primarily to upward ambipolar diffusion caused the electron heating associated with soft particle precipitation. Thus we conclude that care must be taken when inferring lower altitude ionospheric dynamics based on in-situ observations of the ambient plasma from low-Earth orbit. It is a completely unsolved problem of whether most hot patches are formed by precipitation (Oksavik et al., 2006) as opposed as being formed as cold patches and then encountering precipitation later. In general time-dependent modeling is needed to link these perspectives. Examination of a more comprehensive set of events is needed to assess whether this is a common dynamic in the polar ionosphere. The study highlights the need for densely distributed measurements in space and time for understanding ionospheric dynamics in regions subject to complex forcing.

The reported findings are uniquely enabled by the electronic scanning modality of the Advanced Modular ISR (AMISR) radars (PFISR, RISR-N, RISR-C). The forthcoming EISCAT-3D facility will build substantially upon this capability (Stamm, Vierinen, Urco, Gustavsson, & Chau, 2021).

References

Basu, S., & Valladares, C. (1999). Global aspects of plasma structures. *Journal of atmospheric and solar-terrestrial physics*, *61*(1-2), 127–139.

Blelly, P., & Schunk, R. (1993). A comparative study of the time-dependent standard 8-, 13-and 16-moment transport formulations of the polar wind. *AnGeo*, *11*(6), 443–469.

Bonnell, J., Elphic, R. C., Palfery, S., Strangeway, R. J., Peterson, W. K., Klumpar, D., ... McFadden, J. P. (1999). Observations of polar cap arcs on fast. *Journal of Geophysical Research: Space Physics*, *104*(A6), 12669-12681. Retrieved from `https://agupubs.onlinelibrary.wiley.com/doi/abs/10.1029/1999JA900085` doi: https://doi.org/10.1029/1999JA900085

Carlson, H. C. (1994). The dark polar ionosphere: Progress and future challenges. *Radio science*, *29*(1), 157–165.

Carlson, H. C. (2007). Role of neutral atmospheric dynamics in cusp density and ionospheric patch formation. *Geophysical research letters*, *34*(13).

Carlson, H. C. (2012). Sharpening our thinking about polar cap ionospheric patch morphology, research, and mitigation techniques. *Radio Science*, *47*(4).

Coley, W., & Heelis, R. (1998). Structure and occurrence of polar ionization patches.

Journal of Geophysical Research: Space Physics, *103*(A2), 2201–2208.

Crooker, N. U. (1986). An evolution of antiparallel merging. *Geophysical Research Letters*, *13*(10), 1063-1066. Retrieved from `https://agupubs` `.onlinelibrary.wiley.com/doi/abs/10.1029/GL013i010p01063` doi: https://doi.org/10.1029/GL013i010p01063

Crowley, G. (1996). Critical review of ionospheric patches and blobs. *Review of Radio Science 1993–1996*, 619–648.

Dahlgren, H., Perry, G., Semeter, J., St.-Maurice, J.-P., Hosokawa, K., Nicolls, M., ... Heinselman, C. (2012). Space-time variability of polar cap patches: Direct evidence for internal plasma structuring. *Journal of Geophysical Research: Space Physics*, *117*(A9).

Dahlgren, H., Semeter, J., Marshall, R., & Zettergren, M. (2013). The optical manifestation of dispersive field-aligned bursts in auroral breakup arcs. *Journal of Geophysical Research: Space Physics*, *118*(7), 4572–4582.

Davis, C., & McCrea, I. (2004). Estimating uncertainties in incoherent scatter radar parameters from random variations in time series data. In *Annales geophysicae* (Vol. 22, pp. 3523–3529).

De la Beaujardiere, O., Lyons, L., Ruohoniemi, J., Friis-Christensen, E., Danielsen, C., Rich, F., & Newell, P. (1994). Quiet-time intensifications along the poleward auroral boundary near midnight. *Journal of Geophysical Research: Space Physics*, *99*(A1), 287–298.

Dungey, J. W. (1961). Interplanetary magnetic field and the auroral zones. *Physical Review Letters*, *6*(2), 47.

Farley, D. T. (1969). Incoherent Scatter Correlation Function Measurements. *Radio Science*, *4*, 935-953. doi: 10.1029/RS004i010p00935

Fear, R. C., Trenchi, L., Coxon, J., & Milan, S. E. (2017). How much flux does a flux transfer event transfer? *Journal of Geophysical Research: Space Physics*, *122*(12), 12–310.

Fuselier, S., Petrinec, S., & Trattner, K. (2000). Stability of the high-latitude reconnection site for steady northward imf. *Geophysical research letters*, *27*(4), 473–476.

Gillies, R., Perry, G., Koustov, A., Varney, R., Reimer, A., Spanswick, E., ... Donovan, E. (2018). Large-scale comparison of polar cap ionospheric velocities

measured by risr-c, risr-n, and superdarn. *Radio Science*, *53*(5), 624–639.

Gosling, J. T., Thomsen, M. F., Bame, S. J., Elphic, R. C., & Russell, C. T. (1991, August). Observations of reconnection of interplanetar and lobe magnetic field lines at the high-latitude magnetopause. *Journal of Geophysical Research: Space Physics*, *96*(A8), 14097-14106. doi: 10.1029/91JA01139

Heppner, J., & Maynard, N. (1987). Empirical high-latitude electric field models. *Journal of Geophysical Research: Space Physics*, *92*(A5), 4467–4489.

Hones Jr, E., Craven, J., Frank, L., Evans, D., & Newell, P. (1989). The horse-collar aurora: A frequent pattern of the aurora in quiet times. *Geophysical research letters*, *16*(1), 37–40.

Hosokawa, K., Kashimoto, T., Suzuki, S., Shiokawa, K., Otsuka, Y., & Ogawa, T. (2009). Motion of polar cap patches: A statistical study with all-sky airglow imager at resolute bay, canada. *Journal of Geophysical Research: Space Physics*, *114*(A4).

Hosokawa, K., Kullen, A., Milan, S., Reidy, J., Zou, Y., Frey, H. U., . . . Fear, R. (2020, February). Aurora in the Polar Cap: A Review. *Space Science Reviews*, *216*(1), 15. doi: 10.1007/s11214-020-0637-3

Hosokawa, K., Shiokawa, K., Otsuka, Y., Nakajima, A., Ogawa, T., & Kelly, J. (2006). Estimating drift velocity of polar cap patches with all-sky airglow imager at resolute bay, canada. *Geophysical research letters*, *33*(15).

Ismail, S., & Meng, C.-I. (1982). A classification of polar cap auroral arcs. *Planetary and Space Science*, *30*(4), 319–330.

Keiling, A. (2009, February). Alfvén Waves and Their Roles in the Dynamics of the Earth's Magnetotail: A Review. *Space Science Reviews*, *142*(1-4), 73-156. doi: 10.1007/s11214-008-9463-8

Kilcommons, L. M., Redmon, R. J., & Knipp, D. J. (2017). A new dmsp magnetometer and auroral boundary data set and estimates of field-aligned currents in dynamic auroral boundary coordinates. *Journal of Geophysical Research: Space Physics*, *122*(8), 9068–9079.

Koustov, A. V., Ullrich, S., Ponomarenko, P. V., Gillies, R. G., Themens, D. R., & Nishitani, N. (2020). Comparison of superdarn peak electron density estimates based on elevation angle measurements to ionosonde and incoherent scatter radar measurements. *Earth, Planets and Space*, *72*, 1–14.

Kullen, A., Brittnacher, M., Cumnock, J. A., & Blomberg, L. G. (2002, November). Solar wind dependence of the occurrence and motion of polar auroral arcs: A statistical study. *Journal of Geophysical Research (Space Physics)*, *107*(A11), 1362. doi: 10.1029/2002JA009245

Lockwood, M., & Carlson, H. (1992). Production of polar cap electron density patches by transient magnetopause reconnection. *Geophysical research letters*, *19*(17), 1731–1734.

Lockwood, M., & Moen, J. (1999). Reconfiguration and closure of lobe flux by reconnection during northward imf: possible evidence for signatures in cusp/cleft auroral emissions. In *Annales geophysicae* (Vol. 17, pp. 996–1011).

Lu, G., Holzer, T. E., Lummerzheim, D., Ruohoniemi, J. M., Stauning, P., Troshichev, O., ... Parks, G. (2002). Ionospheric response to the interplanetary magnetic field southward turning: Fast onset and slow reconfiguration. *Journal of Geophysical Research: Space Physics*, *107*(A8), SIA 2-1-SIA 2-9. Retrieved from https://agupubs.onlinelibrary.wiley.com/doi/abs/10.1029/2001JA000324 doi: https://doi.org/10.1029/2001JA000324

Lyons, L., Nishimura, Y., Kim, H.-J., Donovan, E., Angelopoulos, V., Sofko, G., ... Nishitani, N. (2011). Possible connection of polar cap flows to pre-and post-substorm onset pbis and streamers. *Journal of Geophysical Research: Space Physics*, *116*(A12).

Ma, Y.-Z., Zhang, Q.-H., Xing, Z.-Y., Heelis, R. A., Oksavik, K., & Wang, Y. (2018). The ion/electron temperature characteristics of polar cap classical and hot patches and their influence on ion upflow. *Geophysical Research Letters*, *45*(16), 8072–8080.

McEwen, D., & Harris, D. (1996). Occurrence patterns of f layer patches over the north magnetic pole. *Radio Science*, *31*(3), 619–628.

Milan, S. E., Hubert, B., & Grocott, A. (2005, January). Formation and motion of a transpolar arc in response to dayside and nightside reconnection. *Journal of Geophysical Research (Space Physics)*, *110*(A1), A01212. doi: 10.1029/2004JA010835

Moen, J., Oksavik, K., Alfonsi, L., Daabakk, Y., Romano, V., & Spogli, L. (2013). Space weather challenges of the polar cap ionosphere. *Journal of Space Weather and Space Climate*, *3*, A02.

Newell, P. T., Feldstein, Y. I., Galperin, Y. I., & Meng, C.-I. (1996). Morphology of nightside precipitation. *Journal of Geophysical Research: Space Physics*, *101*(A5), 10737–10748.

Øieroset, M., Sandholt, P., Denig, W., & Cowley, S. (1997). Northward interplanetary magnetic field cusp aurora and high-latitude magnetopause reconnection. *Journal of Geophysical Research: Space Physics*, *102*(A6), 11349–11362.

Oksavik, K., Moen, J., & Carlson, H. C. (2004, June). High-resolution observations of the small-scale flow pattern associated with a poleward moving auroral form in the cusp. *Geophysical Research Letters*, *31*(11), L11807. doi: 10.1029/2004GL019838

Oksavik, K., Ruohoniemi, J., Greenwald, R., Baker, J., Moen, J., Carlson, H., ... Lester, M. (2006). Observations of isolated polar cap patches by the european incoherent scatter (eiscat) svalbard and super dual auroral radar network (superdarn) finland radars. *Journal of Geophysical Research: Space Physics*, *111*(A5).

Onsager, T., Scudder, J., Lockwood, M., & Russell, C. (2001). Reconnection at the high-latitude magnetopause during northward interplanetary magnetic field conditions. *Journal of Geophysical Research: Space Physics*, *106*(A11), 25467–25488.

Perry, G., Dahlgren, H., Nicolls, M., Zettergren, M., St.-Maurice, J.-P., Semeter, J., ... Chen, S. (2015). Spatiotemporally resolved electrodynamic properties of a sun-aligned arc over resolute bay. *Journal of Geophysical Research: Space Physics*, *120*(11), 9977–9987.

Potemra, T., Zanetti, L., Bythrow, P., Lui, A., & Iijima, T. (1984). By-dependent convection patterns during northward interplanetary magnetic field. *Journal of Geophysical Research: Space Physics*, *89*(A11), 9753–9760.

Redmon, R. J., Denig, W. F., Kilcommons, L. M., & Knipp, D. J. (2017). New dmsp database of precipitating auroral electrons and ions. *Journal of Geophysical Research: Space Physics*, *122*(8), 9056–9067.

Rich, F. J., & Hairston, M. (1994). Large-scale convection patterns observed by dmsp. *Journal of Geophysical Research: Space Physics*, *99*(A3), 3827–3844.

Ruohoniemi, J. M., & Greenwald, R. A. (1998, January). The response of high-latitude convection to a sudden southward IMF turning. *Geophysical research*

letters, *25*(15), 2913-2916. doi: 10.1029/98GL02212

Schunk, R. (1977). Mathematical structure of transport equations for multispecies flows. *Reviews of Geophysics*, *15*(4), 429–445.

Semeter, J., Butler, T., Heinselman, C., Nicolls, M., Kelly, J., & Hampton, D. (2009). Volumetric imaging of the auroral ionosphere: Initial results from pfisr. *Journal of atmospheric and solar-terrestrial physics*, *71*(6-7), 738–743.

Semeter, J., Heinselman, C., Sivjee, G., Frey, H., & Bonnell, J. (2005, November). Ionospheric response to wave-accelerated electrons at the poleward auroral boundary. *Journal of Geophysical Research*, *110*(A9), 11310-+. doi: 10.1029/2005JA011226

Semeter, J., Heinselman, C. J., Thayer, J. P., Doe, R. A., & Frey, H. U. (2003, November). Ion upflow enhanced by drifting F-region plasma structure along the nightside polar cap boundary. *Geophysical Research Letters*, *30*, 3-1. doi: 10.1029/2003GL017747

Semeter, J., & Zettergren, M. (2014). Model-Based Inversion of Auroral Processes. In J. Huba, R. Schunk, & G. Khazanov (Eds.), *Modeling the ionosphere-thermosphere system.* John Wiley & Sons, Ltd, Chichester, UK. doi: 10.1002/9781118704417.ch25

Shiokawa, K., Katoh, Y., Satoh, M., Ejiri, M., Ogawa, T., Nakamura, T., ... Wiens, R. (1999). Development of optical mesosphere thermosphere imagers (omti). *Earth, planets and space*, *51*(7-8), 887–896.

Shiokawa, K., Otsuka, Y., & Ogawa, T. (2009). Propagation characteristics of night-time mesospheric and thermospheric waves observed by optical mesosphere thermosphere imagers at middle and low latitudes. *Earth, planets and space*, *61*(4), 479–491.

Sojka, J. J., Zhu, L., Crain, D., & Schunk, R. W. (1994). Effect of high-latitude ionospheric convection on sun-aligned polar caps. *Journal of Geophysical Research: Space Physics*, *99*(A5), 8851–8863.

Solomon, S. C. (2017). Global modeling of thermospheric airglow in the far ultraviolet. *Journal of Geophysical Research: Space Physics*, *122*(7), 7834–7848.

Stamm, J., Vierinen, J., Urco, J. M., Gustavsson, B., & Chau, J. L. (2021, February). Radar imaging with EISCAT 3D. *Annales Geophysicae*, *39*(1), 119-134. doi: 10.5194/angeo-39-119-2021

744 Strangeway, R. J., Russell, C. T., Carlson, C. W., McFadden, J. P., Ergun, R. E.,

745 Temerin, M., . . . Moore, T. E. (2000). Cusp field-aligned currents and ion

746 outflows. *Journal of Geophysical Research: Space Physics*, *105*(A9), 21129-

747 21141. Retrieved from https://agupubs.onlinelibrary.wiley.com/doi/

748 abs/10.1029/2000JA900032 doi: https://doi.org/10.1029/2000JA900032

749 Tsunoda, R. T. (1988). High-latitude f region irregularities: A review and synthesis.

750 *Reviews of Geophysics*, *26*(4), 719–760.

751 Valladares, C., Carlson Jr, H., & Fukui, K. (1994). Interplanetary magnetic field

752 dependency of stable sun-aligned polar cap arcs. *Journal of Geophysical Re-*

753 *search: Space Physics*, *99*(A4), 6247–6272.

754 Valladares, C., Decker, D., Sheehan, R., Anderson, D., Bullett, T., & Reinisch, B.

755 (1998). Formation of polar cap patches associated with north-to-south tran-

756 sitions of the interplanetary magnetic field. *Journal of Geophysical Research:*

757 *Space Physics*, *103*(A7), 14657–14670.

758 Watanabe, M., Kabin, K., Sofko, G. J., Rankin, R., Gombosi, T. I., Ridley, A. J.,

759 & Clauer, C. R. (2005). Internal reconnection for northward interplanetary

760 magnetic field. *Journal of Geophysical Research: Space Physics*, *110*(A6).

761 Weimer, D. (1995). Models of high-latitude electric potentials derived with a least

762 error fit of spherical harmonic coefficients. *Journal of Geophysical Research:*

763 *Space Physics*, *100*(A10), 19595–19607.

764 Zettergren, M., Lynch, K., Hampton, D., Nicolls, M., Wright, B., Conde, M., . . .

765 Powell, S. (2014). Auroral ionospheric f region density cavity formation and

766 evolution: Mica campaign results. *Journal of Geophysical Research: Space*

767 *Physics*, *119*(4), 3162–3178.

768 Zettergren, M., & Semeter, J. (2012). Ionospheric plasma transport and loss in auro-

769 ral downward current regions. *Journal of Geophysical Research: Space Physics*,

770 *117*(A6).

771 Zettergren, M., Semeter, J., & Dahlgren, H. (2015). Dynamics of density cavities

772 generated by frictional heating: Formation, distortion, and instability. *Geo-*

773 *physical Research Letters*, *42*(23), 10–120.

774 Zettergren, M., & Snively, J. (2013). Ionospheric signatures of acoustic waves gen-

775 erated by transient tropospheric forcing. *Geophysical Research Letters*, *40*(20),

776 5345–5349.

Zettergren, M., & Snively, J. (2015). Ionospheric response to infrasonic-acoustic waves generated by natural hazard events. *Journal of Geophysical Research: Space Physics*, *120*(9), 8002–8024.

Zhang, Q.-H., Ma, Y.-Z., Jayachandran, P., Moen, J., Lockwood, M., Zhang, Y.-L., ... others (2017). Polar cap hot patches: Enhanced density structures different from the classical patches in the ionosphere. *Geophysical Research Letters*, *44*(16), 8159–8167.

Zhang, Q.-H., Moen, J., Lockwood, M., McCrea, I., Zhang, B.-C., McWilliams, K. A., ... others (2016). Polar cap patch transportation beyond the classic scenario. *Journal of Geophysical Research: Space Physics*, *121*(9), 9063–9074.

Zou, Y., Nishimura, Y., Burchill, J. K., Knudsen, D. J., Lyons, L. R., Shiokawa, K., ... others (2016). Localized field-aligned currents in the polar cap associated with airglow patches. *Journal of Geophysical Research: Space Physics*, *121*(10), 10–172.

Zou, Y., Nishimura, Y., Lyons, L. R., Shiokawa, K., Donovan, E. F., Ruohoniemi, J. M., ... Nishitani, N. (2015). Localized polar cap flow enhancement tracing using airglow patches: Statistical properties, imf dependence, and contribution to polar cap convection. *Journal of Geophysical Research: Space Physics*, *120*(5), 4064-4078. Retrieved from `https://agupubs.onlinelibrary.wiley.com/doi/abs/10.1002/2014JA020946` doi: https://doi.org/10.1002/2014JA020946